Artical ID:1006-3471(2010)03-0244-11

Phenomena Characterization of Energy Materials by X-ray Absorption Spectroscopy

CHENG Ming-yao[1], PAN Chun-jen[2], CHENG Ju-hsiang[2], HWANG Bing-joe[2,3*]
(1. *Graduate Institute of Engineering, Taiwan University of Science and Technology, Taipei* 106, *Taiwan, China*;
2. *Department of Chemical Engineering, Taiwan University of Science and Technology, Taipei* 106, *Taiwan, China*;
3. *Synchrotron Radiation Research Center, HsinChu* 300, *Taiwan, China*)

Abstract: The aim of this review is to introduce the characterization of energy materials by X-ray absorption spectroscopy (XAS). This technique allows us to probe changes in the valance state and the local environment of the targeted element in the active material; thereby, leading to a better understanding of its electrochemical behavior, and hopefully showing the way to improved performance. Here, electrocatalysts for fuel cells and active electrode materials for Li-ion batteries are taken as the examples that illustrate the capability of XAS and allow observation and theory to be correlated with electrochemical phenomena.

Key words: X-ray absorption spectroscopy; nanoparticles; bimetallic; Li-ion battery; electrode
CLC Number: O646; TN14 **Document Code**: A

1 Introduction

Recently environmental issues have driven dozens of researches worldwide to pursue efficient and clean energy technologies for a better quality of life. Several renewable clean energy technologies have been developed. The performance of these devices is influenced by several factors: one of the most critical issues is the characteristics of the electrode materials, which dominates the reaction kinetics and the corresponding stabilities of the devices. Currently material characterization techniques are able to provide multi-scale information and lead us a better understanding of the physical and chemical properties that underlie electrochemical behavior. However, the change of local environment from the atomic level to the ~1 nm scale is difficult to probe with most state-of-the-art techniques. Although modern transmission electron microscopy (TEM) can provide excellent atomic scale structural (HRTEM, STEM) and composition (STEM + EDS) information, difficulties in sample preparation together with limitations with respect to the analysis environment restrict their use in various investigations. X-ray absorption spectroscopy (XAS) is able to provide detailed local structural information in the scale range below 1 nm. The information gathered is representative since it is taken from the averaged spectra, obtained using the required quantity of the sample; it should therefore follow Beer's law. A significant area of application for XAS exploits its capability for *in situ* analysis, where the use of a synchrotron radiation-based X-ray source allows for the easy design of *in situ* monitoring experiments to detect changes in materials during cell operation. The unique advantage of XAS leads to a clear picture of material transformation in terms of structure, composition and valence state of the element.

Received: 2010-07-18, Revised: 2010-07-29 * Corresponding author: E-mail: bjh@ mail. ntust. edu. tw

2　X-ray Absorption Spectroscopy (XAS)

To understand the capability of XAS, its origin should be briefly addressed. In general the interactions of X-rays with matter can be divided into absorption and scattering. X-ray scattering includes elastic and inelastic scattering. In the elastic case, microstructural information can be determined, either for soft or crystalline solids. In the case of inelastic scattering and absorption, the electronic structure and the local environment of the targeted element can be probed. The X-ray absorption spectroscopy (XAS) technique was developed based on the fundamentals of X-ray-matter interactions, in which the absorption of the X-ray at a specific energy (edge) by the core-level electron (K, L, M shells) of an atom takes place and the excited electron will be ejected from the atom as an electron wave. This is the basis of photoelectric absorption, where the specific energy is the (K, L or M) edge of the target element. The electron wave can interact with the atoms nearby the central atom that the excited electron comes from, so that its properties can be altered by the surrounding atoms (Fig. 1). It is crucial to remember that XAS probes the changes in the local structure that surrounds the targeted atom. This simple description of the process, starting with an X-ray being absorbed by an atom, briefly illustrates the basics of the XAS technique. Basically XAS can be divided into two parts: X-ray absorption near-edge spectroscopy (XANES) and extended X-ray absorption fine structure (EXAFS), which provides different information with respect to the analyzed materials and will be illustrated in detail in the following paragraphs.

During the experiment, the energy of the incident X-ray increases, from a level at which it is not absorbed by the targeted atom (pre-edge), this is followed by a transient step from the background (without absorption), to the absorption stage (the so-called the near edge, XANES region) and the EXAFS region. The electronic structure (*d*-band vacancy, valence state) and the coordination symmetry of the targeted atom (the atom that absorbed the incident X-ray) in the sample determine the features of XANES. Basically the shift of the edge position (white line) can be taken as a guideline for the change of the valence state of the absorbing atom, which can be roughly determined by the linear combination of the edge positions of the standard samples with the known valence states. In some cases the height and the position of the peak appearing at the pre-edge region also reveals the oxidation state of the absorbing atom. However, XANES is difficult to fully interpret since there is no a simple equation to describe the feature. Even first-principle calculations to adequately explain XANES are not yet fully developed.

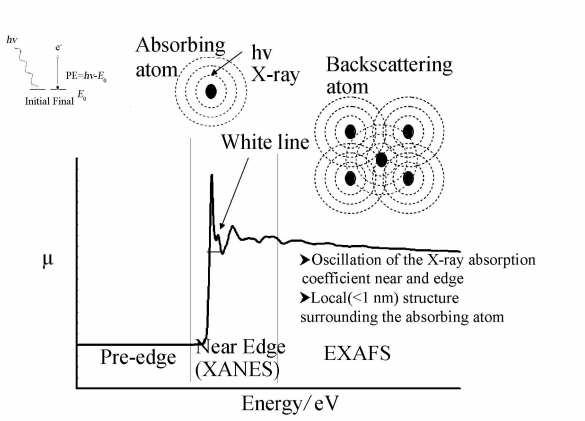

Fig. 1　Explanation of a typical XAS

The region of EXAFS extends from 50 to 1000 eV after edge. A typical feature of the spectrum in the EXAFS region composes of several oscillations. The origin of the oscillations comes from the interference of outgoing and backscattered photoelectron waves, which may interfere either constructively or destructively, depending on the ratio of λ (wavelength of photoelectron) and R (distance between the absorbing atom and the surrounding scattering atoms). The change of λ is due to the change of the incident X-ray energy during XAS measurement. Therefore the interference between the outgoing and backscattered photoelectron waves modifies X-ray absorption, resulting in the oscillations in EXAFS region. The frequency of the oscillation is associated with R, and the amplitude

is correlated with the number and type of neighboring atoms. With a proper model and a data reduction process, local structural information in terms of the coordination number and the bond distance can be obtained, these parameters are related by the EXAFS equation:

$$\chi(k) = \sum_j \frac{N_j f_j(k) e^{-2k^2\sigma_j^2}}{kR_j^2} \sin[2kR_j + \delta_j(k)] \quad (1)$$

$$k = \sqrt{\frac{2m(E - E_0)}{h^2}} \quad (2)$$

Where:

$\chi(k)$ is the EXAFS signal; k is the wave number; m the photoelectron mass; E is the X-ray energy; E_0 is the energy at the edge of absorbing element; h is the Planck constant; N is the coordination number; $f(k)$ is the scattering factor; $\delta(k)$ is the phase shift; R is the bond distance; and σ^2 is the mean-square disorder of neighbor distance.

Since $f(k)$ and $\delta(k)$ are related to the atomic number Z of the scattered atom, we can determine the identities of neighboring atoms. If the above information is known, N, R and σ^2 can also be obtained. In many cases, the changes in the local structural parameters can be correlated with the electrochemical behavior of the materials. Our group has had a long-term interest in the application of XAS analysis, especially to fuel cell electrocatalysts and the cathode materials used in Li-ion batteries. Some general strategies have been developed for probing these materials, which strongly correlates the measured parameters with their performance. In this review we have illustrated the application of XAS to energy related materials, and in doing so we hope to have provided some useful information for readers.

2.1 Characterization of Nanostructure of Bimetallic Nanoparticles

Bimetallic nanoparticles (NPs) are of great interest from both the scientific and technological perspectives. The physical and chemical properties of bimetallic NPs, such as their: (i) homogeneity, (ii) surface segregation, (iii) structure and shape, and (iv) the extent of alloying or atomic distribution; play a crucial role with respect to their catalytic behavior. A general methodology, based on XAS, to determine the alloying extent and the atomic distribution in bimetallic NPs was developed by our group[1]. These local structural parameters have been employed to resolve the properties of the bimetallic NPs. The strategy, we have developed, will be carefully discussed with reference to a simple bimetallic (A-B) NP model.

To reach the target, some parameters need to be derived, based on N (their coordination number), these include: P_{observed}, R_{observed}, P_{random}, and R_{random}. The parameter P_{observed} is defined as the ratio of the scattering atoms B coordination number around the absorbing A atoms ($N_{\text{A-B}}$) to the total coordination number of the absorbing atoms ($\sum N_{\text{A-}i}$) ($P_{\text{observed}} = N_{\text{A-B}} / \sum N_{\text{A-}i}$). Similarly, R_{observed} can be defined as $R_{\text{observed}} = N_{\text{B-A}} / \sum N_{\text{B-}i}$. On the other hand, P_{random} and R_{random} can be taken as 0.5 for perfectly alloyed bimetallic NPs if the atomic ratio of A to B is 1∶1. This value can be deduced from the fact that $N_{\text{A-A}} = N_{\text{A-B}}$ and $N_{\text{B-B}} = N_{\text{B-A}}$, for perfectly alloyed bimetallic NPs and can be easily extended to the other NP systems of interest. For example, in the case of A-B bimetallic NPs with an atomic ratio of 1∶2 (A∶B), $2N_{\text{A-A}} = N_{\text{A-B}}$ and $N_{\text{B-B}} = 2N_{\text{B-A}}$ are easily understood for perfect alloyed bimetallic NPs, indicating values of 0.67 for P_{random} and 0.33 for R_{random}. Here, we focus on the 1∶1 bimetallic NP system. From the ratio of P_{observed} to P_{random}, the alloyed extent of element A (J_{A}) in NPs is able to be evaluated, as well as the ratio of R_{observed} to R_{random} for that of element B (J_{B}) in NPs, this is shown by Equations (3) and (4), respectively.

$$J_{\text{A}} = \frac{P_{\text{observed}}}{P_{\text{random}}} \times 100\% \quad (3)$$

$$J_{\text{B}} = \frac{P_{\text{observed}}}{P_{\text{random}}} \times 100\% \quad (4)$$

To facilitate a better understanding, schematic models of various atomic distributions in the A-B bimetallic NPs are presented to illustrate the relationship between $\sum N_{\text{A-}i}$, $\sum N_{\text{B-}i}$, J_{A}, and J_{B} (Fig. 2). With the aid of the alloyed extents, as well as the

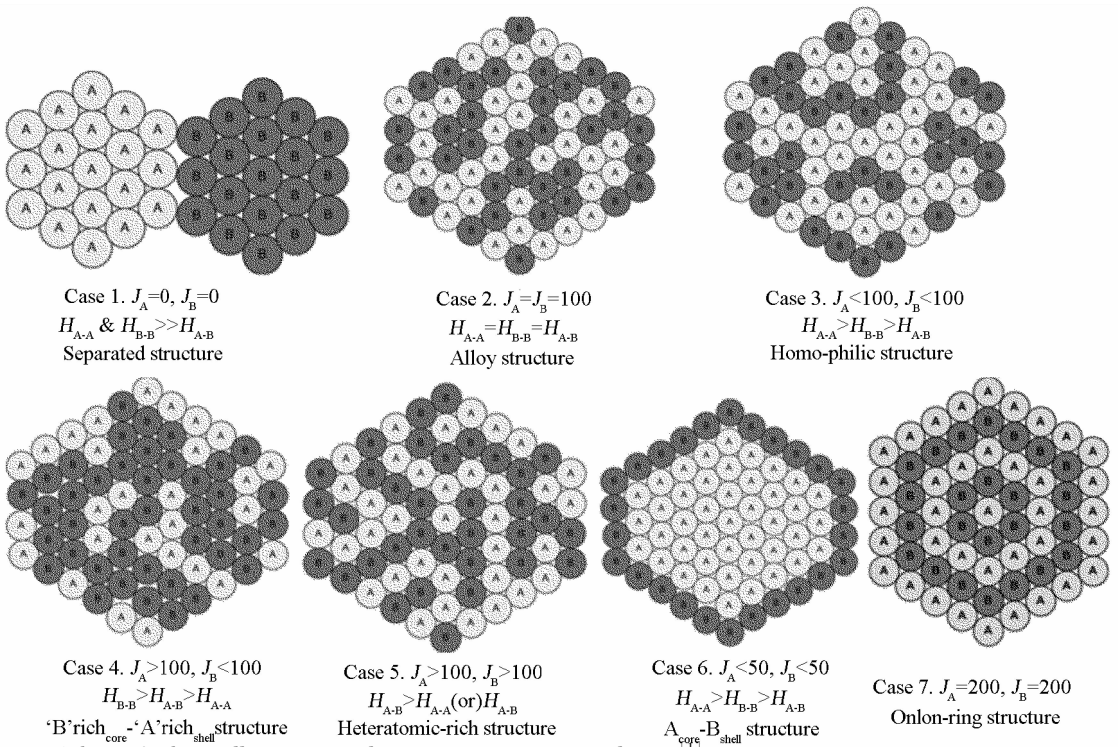

Fig. 2　Scheme for bimetallic nanoparticles at various atomic populations[1]

structural parameters extracted from EXAFS, the structure of the NPs (atomic population) is able to be predicted, by analogy to seven general cases- this will be discussed in the following paragraphs. In Case 1, if $J_A = 0$ and $J_B = 0$, then neither the A or B particles are involved in alloying, this results in separated cluster particles (see Fig. 2, Case 1). If N_{A-A} equals to N_{B-B}, the particle size of both A and B is the same. For $N_{A-A} > N_{B-B}$ it reveals the particle size of A is larger than that of B. Further, the homoatomic interactions of A atoms (H_{A-A}) and of B atoms (H_{B-B}) are much greater than the bimetallic (A-B) heteroatomic interactions (H_{A-B}), indicating no heteroatomic interactions in the NPs.

In Case 2, $J_A = J_B = 100\%$, both A and B atoms are involved completely in the alloying process, resulting in perfectly alloyed NPs (see Fig. 2, Case 2). If the bimetallic system is in the equilibrium state, then the interactions will be $H_{A-A} = H_{B-B} = H_{A-B}$, which means that there are equal bimetallic interactions in the NPs.

If $J_A < 100\%$ and $J_B < 100\%$ as shown in Case 3 of Fig. 2, then neither the A or B atoms are preferentially alloyed. The NPs show more homoatomic interactions (A-A and B-B) than heteroatomic interactions (A-B). Once J_B is larger than J_A, it appears that the core is A-rich and the shell is B-rich in the NPs. In other words, $\sum N_{A-i}$ is greater than $\sum N_{B-i}$ and the order of interactions will be $H_{A-A} > H_{B-B} > H_{A-B}$. If $J_A > 100\%$ and $J_B < 100\%$ (Case 4), B atoms prefer B atoms rather than A atoms, but A atoms prefer B atoms rather than A atoms. As a result, the atomic distribution of A atoms is better than that of B atoms, indicating less segregation of A atoms than that of B atoms. In the equilibrium state, the interactions are in the following order: $H_{B-B} > H_{A-B} > H_{A-A}$. Here, the bimetallic NPs adopt a structure similar to that of the B rich in core and A rich in shell (see Fig. 2, Case 4), implying $\sum N_{B-i} > \sum N_{A-i}$. Even though the structures described in Cases 3 and 4 are similar in nature, the atomic dispersion of A in the NPs of Case 4 is better, and cannot simply be obtained from the coordination numbers. If $J_A < 100\%$ and $J_B > 100\%$, the situation is opposite to the Case 4.

In Case 5 ($J_A > 100\%$ and $J_B > 100\%$), both the atomic distributions of A and B atoms are much improved, and the resulting structure can be expected

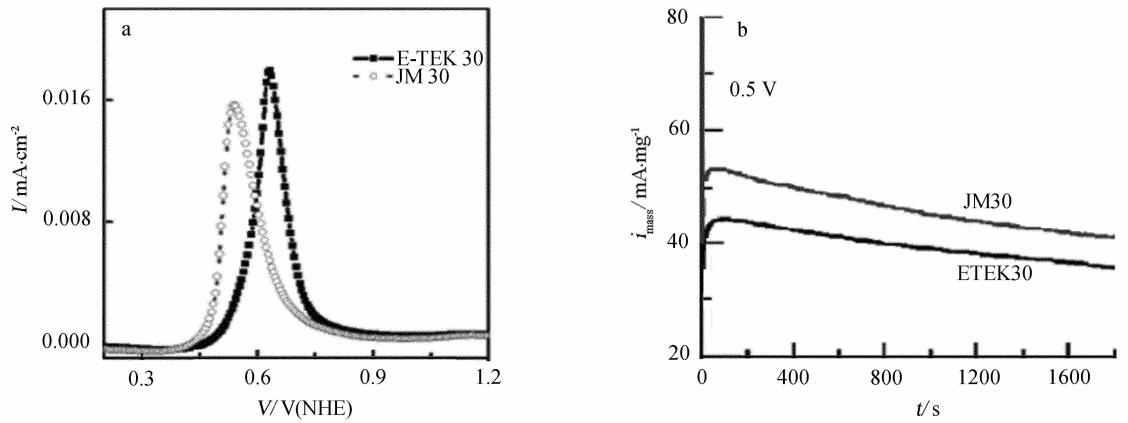

Fig. 3 Comparison of methanol oxidation activity of JM-30 and E-TEK 30 Pt-Ru/C catalysts

a. CO stripping voltammograms recorded in 0.5 mol · L^{-1} H_2SO_4 solution (CO gas was purged for 15 min at 0.1 V and then stripped); b. chronoamperometric analysis at constant potential 0.5 V versus NHE in 15% CH_3OH + 0.5 mol · L^{-1} H_2SO_4 [1]

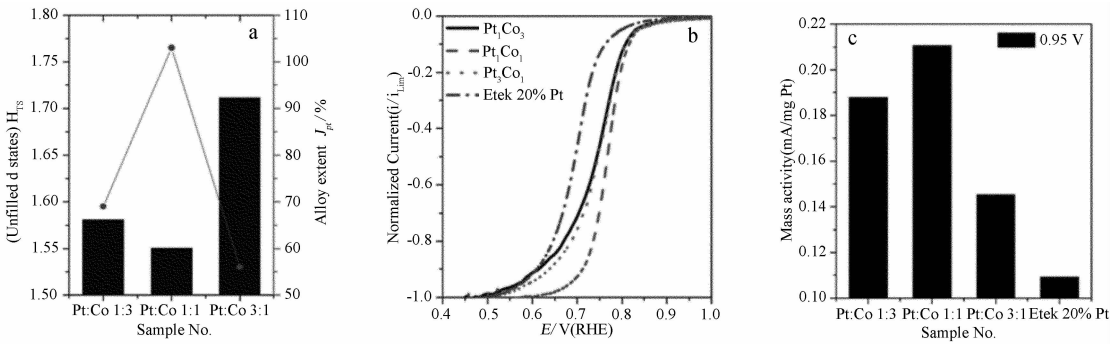

Fig. 4 Properties and oxygen reduction reaction (ORR) activity of homemade Pt-Co electrocatalyst

a. d-band unfilled state and extent of platinum alloying; b. linear sweep voltammograms recorded at 1 mV · s^{-1} for ORR; c. mass-activity of ORR measured at 0.95 V (vs RHE) of (b) [4]

to be show more heteroatomic interactions than homoatomic interactions (see Fig. 2, Case 5). At equilibrium, the interactions will be in the following order: $H_{A\text{-}B} > H_{A\text{-}A}$ and $H_{A\text{-}B} > H_{B\text{-}B}$. By comparing the different models described above (from Cases 3 to 5), we can provide quantitative atomic distribution, which can be very important for NP applications. In Case 6 ($J_A < 50\%$ and $J_B < 50\%$) the resultant structure shows A particles are in the core and B particles are in the shell (see Fig. 2, Case 6). The total coordination number, $\sum N_{A\text{-}i}$, will be greater than that of $\sum N_{B\text{-}i}$. At equilibrium, the interactions follow the order: $H_{A\text{-}A} > H_{B\text{-}B} > H_{A\text{-}B}$. In Case 7 ($J_A = 200\%$ and $J_B = 200\%$), A atoms always prefer B atoms and vice versa, and the resulting structure looks like an onion ring (see Fig. 2, Case 7), in which one layer is occupied by A atoms and the other layer by B atoms.

The above discussion shows a general strategy to describe the atomic distribution based on XAS analysis and the developed J factor. The following paragraphs adopt this strategy to correlate the atomic population of bimetallic NPs to the corresponding electrocatalytic performance.

2.2 Atomic Population of Pt-Ru Bimetallic Electrocatalysts Toward Methanol Oxidation Ability

The atomic populations of bimetallic NPs are crucial to their electrocatalytic performance; this is the case even for materials having the same overall composition. To demonstrate this point, we will show the correlation between the performance and the corresponding alloyed extent, for both commercially available E-TEK 30 (30%, by mass, Pt-Ru on carbon, Pt: Ru = 1: 1) and JM-30 (30%, by mass, Pt-Ru on car-

bon, Pt: Ru = 1: 1)[1]. The atomic population is extremely important for Pt-Ru electrocatalysts in the methanol oxidation reaction (MOR), since surface Ru is thought to provide hydroxyl groups via H_2O hydrolysis, which is the key to CO poisoning at Pt active sites. To reach the maximum MOR ability, higher alloyed extents of Pt-Ru are preferred. The alloyed extent of Pt(J_{Pt}) and Ru(J_{Ru}) in E-TEK 30 are 26% and 48%, respectively. For JM-30 catalyst, J_{Pt} and J_{Ru} are 40% and 78%, respectively. Clearly, both catalysts show considerable amounts of Ru segregated on the shell layer, similar to Case 3. However the degree of Ru segregation for E-TEK 30 is higher than that of JM-30, since JRu for JM-30 indicates a better alloyed extent of Ru at the shell. The different atomic populations for both catalysts directly reflect on their electrochemical catalytic performance, where a better alloyed extent of Ru for JM-30 exhibits a higher activity toward methanol oxidation as well as the CO striping ability (Fig. 3). Similar work done on the Pt-Ag system is shown in our previous publication[2], in which our strategy of using XAS-based analysis, as a general probe, was directed towards the understanding of bimetallic electrocatalysts.

It is worth noting that the surface population of the Pt-Ru electrocatalyst can be altered by annealing in a hydrogen or oxygen atmosphere, depending on the strength of the interactions between H_2 (O_2) molecules and Pt (Ru) atoms, respectively; determining which will be driven from core/surface to surface/core. The phenomena can also be probed by the developed XAS-based analysis[3].

2.3 Bimetallic Pt-Co Electrocatalysts for Oxygen Reduction Reaction

Currently the oxygen reduction reaction (ORR) is one of the most important issues needing to be addressed with respect to fuel cell commercialization. Slow ORR kinetics as well as high Pt usage has stimulated a worldwide investigation for better materials. Bimetallic NPs may show a way to address the slow ORR kinetics of Pt. Basically, the introduction of Pt-M based electrocatalysts modifies the electronic structure of Pt (by reducing the unfilled d-state of Pt), which leads to weaker adsorption of O atoms at Pt active sites, and makes the subsequent reduction of O atoms easier. Therefore, M core-Pt shell-like bimetallic NPs are preferred, since all Pt atoms can serve as reaction sites and the core M atoms underneath are able to modify the electronic structure of the surface Pt atoms. Nevertheless NPs with Pt monolayers on M cores should provide significant benefits in terms of proper electronic structure and less usage of Pt. Again the atomic population of the bimetallic Pt-M NPs plays a key role, which can be probed by the developed XAS-based strategy.

For example, Pt-Co is a promising electrocatalyst for ORR, which has been thoroughly investigated by our team[4]. The variation in unfilled d-states (H_{Ts}) of the in-house fabricated Pt_xCo_{1-x}/C bimetallic NPs with various Pt-to-Co ratios is depicted in Fig. 4. The H_{Ts} values in the case of samples containing higher Co contents, that is, Pt_1Co_3/C and Pt_1Co_1/C bimetallic NPs, are lower than those of the reference Pt foil (H_{Ts} = 1.6). The observed trend might be due to the enhanced hybridization between Co (3d) and Pt (5d), i. e. the electron density of Co (3d) reduces and contributes to Pt (5d). It is worth mentioning that the tendency of the variations in H_{Ts} is consistent with J_{Pt} in Pt-Co nanoparticles. The higher J_{Pt} value observed in the case of Pt_1Co_1/C, the greater is the Pt alloying with Co. The enhanced ORR performance of Pt_1Co_1/C is partially attributed to the comparatively higher alloyed extent of Pt and Co, which results in higher numbers of Pt with lower unfilled d-states. A similar situation is observed for the Pt_xFe_{1-x}/C system: the Pt_1Fe_1/C, which is the lowest unfilled d-state value and highest alloyed extent of Pt, contributes to the enhanced ORR performance[5].

The dealloying behavior Co, from Pt-Co/C bimetallic nanoparticles, usually takes place during the ORR in acidic conditions. Therefore the formation of core-shell like Pt-Co NPs with a Pt skin on the Pt-Co surface is desired to prevent from further Co loss and to provide a better surface Pt catalytic activity towards ORR. Here we try to analyze the phenomena, via the acidic treatment of homemade Pt-Co/C, using XAS and

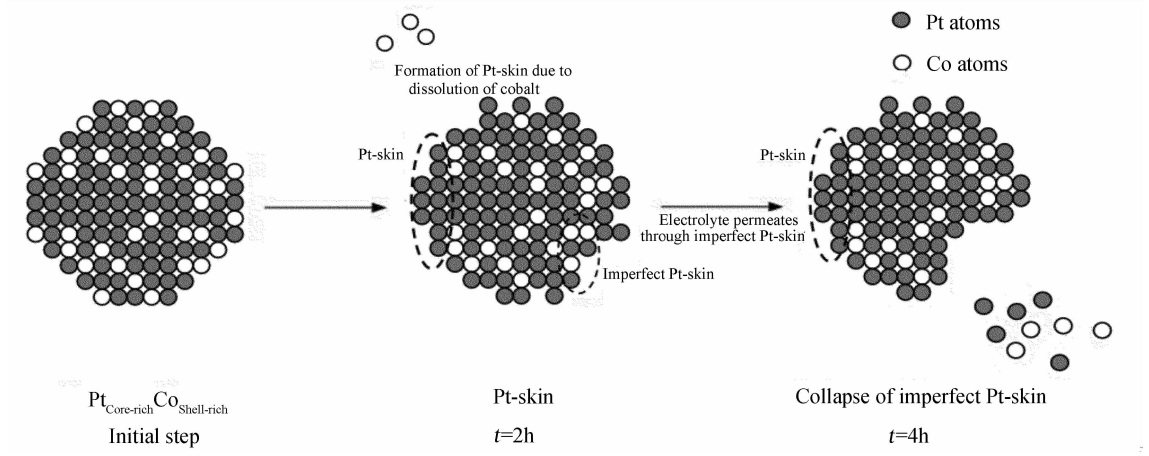

Fig. 5 Proposed dealloying mechanism for Pt-Co NPs[6]

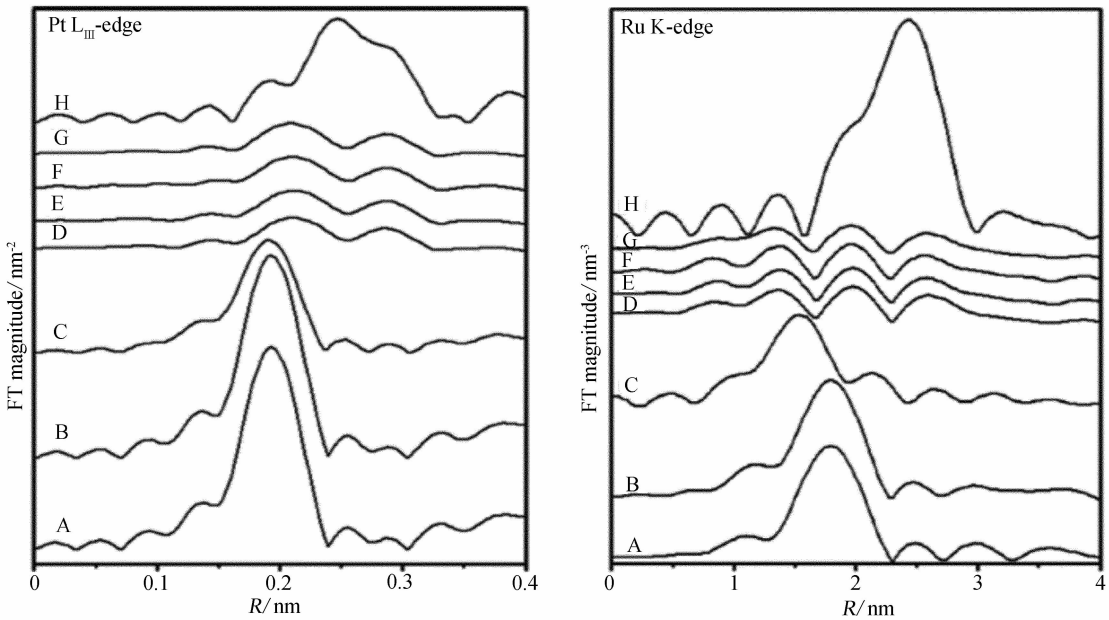

Fig. 6 Pt L_{III}-edge(a) and Ru K-edge (b) FT-EXAFS spectra at various reaction steps during the formation of Pt-Ru nanoparticles by polyol method
A. 0.25 mol · L^{-1} H_2PtCl_6 in ethylene glycol (EG), B. 0.25 mol · L^{-1} H_2PtCl_6 + 0.25 mol · L^{-1} $RuCl_3$ in EG, C. increase pH value to 11, D. reflux at 160 ℃, 0.5 h, E. reflux at 160 ℃, 1 h, F. reflux at 160 ℃, 2 h, G. reflux at 160 ℃, 4 h, H. Pt (or Ru) foil[7]

propose a dealloying mechanism for Pt-Co NPs (Fig. 5). It is proposed that an imperfect Pt skin on the Pt-Co NPs will further suffer from the loss of Co, which leads to collapse of the NPs[6].

2.4 *In situ* Observation of Pt-Ru NPs Formation by Polyol Process

One of the most significant benefits of the XAS technique is its capability for *in situ* probing analysis. We have resolved the polyol process for the formation of Pt-Ru NPs using XAS[7]. It is able to provide a clear picture for the evolution of NPs (Fig. 7), making further improvement/modification of the NPs relatively easy. H_2PtCl_6 and $RuCl_3$ were used as the precursors and dissolved in ethylene glycol (EG). Subsequently the pH of the solution was increased to 11, which was followed by refluxing at 160 ℃. Fig. 6 shows the respective Pt L_{III}-edge and Ru K-edge Fourier transforms of EXAFS of the precursor solution during the polyol process. Clearly, the environment of Pt at step (A) and (B) is similar. The peak at

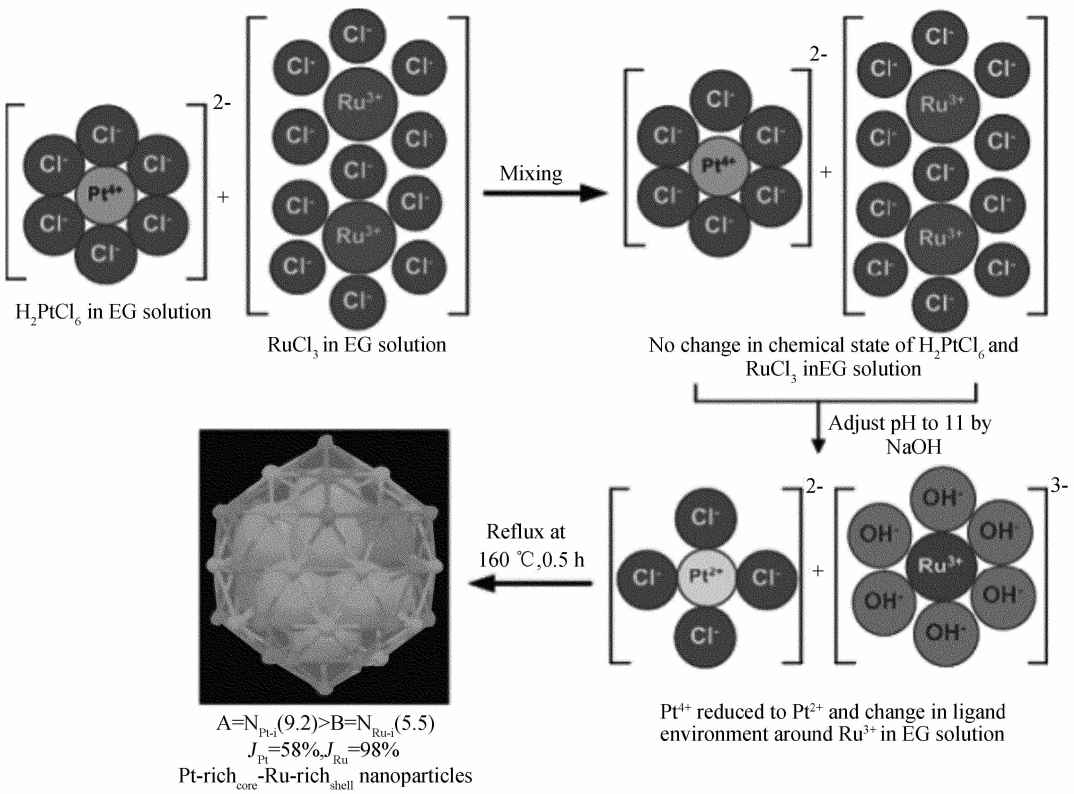

Fig. 7　Proposed reaction mechanisms for the formation of Pt-Ru/C NPs by polyol method[7]

around 0. 2 nm in FT-EXAFS is attributed to Pt-Cl bond (without phase correction). Similar behavior is observed for Ru K-edge FT-EXAFS. Once the solution pH reaches 11, the environment changes rapidly, this can be clearly deduced from FT-EXAFS since the peak intensity (Pt) and position (Ru) obviously change. It is proposed that the valence state of Pt changes from 4 + to 2 +, while the Ru-Cl bond is replaced by Ru—OH at pH = 11. The subsequent refluxing step lead to the reduction of Pt^{4+} and Ru^{3+} to metal atoms within 0. 5 h, which can be identified from the position of their peaks being similar to those of bulk Pt and Ru foils. It is noted that the reduction of Pt^{4+} and Ru^{3+} is a function of EG, which acts as the solvent as well as the reduction agent. The weak peak intensity indicates low coordination numbers for both Pt and Ru, resulting from the average of the surface and the inner atoms and can be taken as an indicator of the nano-sized particles nature. The J factors for both Pt (J_{Pt} = 58%) and Ru (J_{Ru} = 98%) of the synthesized Pt-Ru NPs are determined from the fitting results and indicate a Pt-rich core and a Ru-rich shell. This can be easily explained from the higher standard reduction potential of $PtCl_4^{2-}$ than of Ru $(OH)_6^{3-}$, which facilitates Pt cluster formation to give the nuclei for the further reduction of residual Pt^{2+} and Ru^{3+}.

The above strategy has been applied to various bimetallic NPs-related investigations[8-11], indicating the capability of the developed XAS-based technique for probing the atomic population, which can be elegantly correlated with their electrocatalytic performance.

2. 5　Variation of Structure of Cathode Materials during Electrochemical Cycling

In situ XAS has also been employed to examine the electronic and local structures of transition metal ions in the cathodes of Li-ion batteries. The absorption peak features of the transition metal K-edge XAS provide useful structural information, such as: the oxidation state of chemical species, their site symmetries, and covalent bond strengths. During charging/discharging processes, the active element can be easily probed

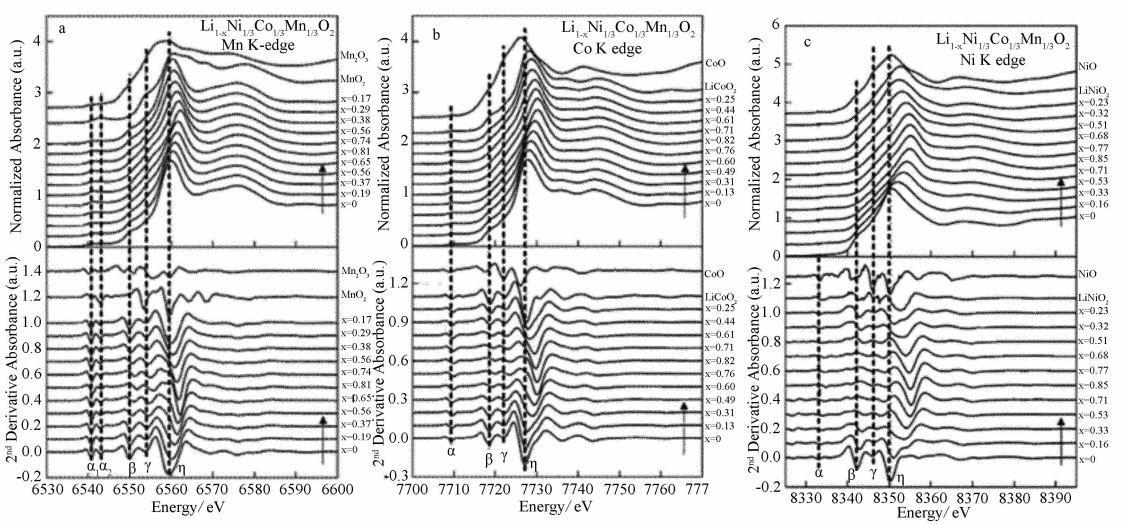

Fig. 8 Normalized and second derivative XANES of Mn K-edge(a), Co K-edge (b), and Ni K-edge (c) for $Li_{1-x}Ni_{1/3}Co_{1/3}Mn_{1/3}O_2$ at various degrees of charge state during first charge and discharge cycle[12]

since the change of the valence state of the active element can be resolved in real-time. Further the changes of bond distance around the absorbing atom during charging/discharging are able to be examined, which may reveal possible pathways for Li^+ extraction/intercalation. Here we take $Li_{1-x}Ni_{1/3}Co_{1/3}Mn_{1/3}O_2$ as examples to illustrate how the developed XAS analysis technique works[12].

For the pristine $Li_{1-x}Ni_{1/3}Co_{1/3}Mn_{1/3}O_2$ compound ($x=0$), the edge position for the Mn, Co, and Ni K-edges can be confirmed with XANES (not shown) as being almost the same as those of the references: MnO_2 (Mn^{4+}), $LiCoO_2$ (Co^{3+}), and NiO (Ni^{2+}), respectively, suggesting the same oxidation states of the selected absorbing atoms as +4 for Mn, +3 for Co, and +2 for Ni in the pristine material.

To monitor the changes in real-time of $Li_{1-x}Ni_{1/3}Co_{1/3}Mn_{1/3}O_2$ during Li^+ extraction and insertion, in situ Mn, Co and Ni K-edge XANES spectra were analyzed (Fig. 8). Clearly, the obvious alteration of the Mn K-edge XANES feature is shown at various degrees of charge state, indicating the changes to the Mn local environment. However, the edge position does not show a clear shift, indicating the constant valence state of Mn during the charging and discharging process. The fact can also be deduced from the peaks $\alpha 1$ and $\alpha 2$, since they are invariant as well. The intensities of both the β and η peaks, corresponding to 1s $\rightarrow$4p transitions, results from a shakedown process and without the shakedown process, they become weaker upon charging. This may be due to the small decrease of p character by Mn 3d-4p orbital mixing.

A clear change of the Co K-edge XANES spectra at various degree of charging states are shown in Fig. 8b. With continuous extraction of Li ions from the electrode, the absorption intensities of the two peaks β and η decrease with the degree of charge state. This may be due to the distortion of the CoO_6 octahedron structure associated with slight decrease of p character resulting from Co 3d-4p orbital mixing. Also, the shift of the ε peak toward higher energies indicates the change of local symmetry. The energy positions of the pre-edge peak α and the absorption edge are almost identical during extraction and reinsertion of Li^+, which implies Co is not the active element in $Li_{1-x}Ni_{1/3}Co_{1/3}Mn_{1/3}O_2$.

On the contrary, the absorption edge (white line) of Ni K-edge XANES spectra is sensitive to the degree of charge state (Fig. 8c). Initially the energy positions of the pre-edge peak α and the absorption edge β for the pristine $LiNi_{1/3}Co_{1/3}Mn_{1/3}O_2$ are similar to those of the reference NiO, indicating the valence state of +2 for Ni. Upon delithiation, these peaks gradually shift toward higher values and ultimately reach absorption energies higher than those in $LiNiO_2$ for $x>0.85$. These peaks reversibly shift back to low-

er energies upon lithiation. This behavior suggests the redox pair reactions proceed by, either: a two-step reaction composed of Ni^{2+}/Ni^{3+} and then Ni^{3+}/Ni^{4+}, or a one-step reaction of Ni^{2+}/Ni^{4+}, might take place during charging and discharging. It is worth noting that the XANES feature of $Li_{1-x}Ni_{1/3}Co_{1/3}Mn_{1/3}O_2$ at $x = 0.33$ is in agreement with that of the reference $LiNiO_2$, corresponding to a transition state from Ni^{2+} to Ni^{3+} upon charging. However the feature is still observed at the end of discharging, indicating the irreversible capacity that results from part of Ni^{3+} not being able to be reduced to Ni^{2+}. After the first cycle it is evident that there will not be a full recovery of the Ni K-edge absorption energy shift.

The change of local structure at the respective Mn, Co and Ni K edges is related by the extracted structure parameter from the EXAFS regions. The correlations between bond length (or Debye-Waller factor) and the degree of charge state are analyzed by shells. The changes of the first shell (Mn—O, Co—O, and Ni—O) in $Li_1Ni_{1/3}Co_{1/3}Mn_{1/3}O_2$ during various charging states are shown in Fig. 9. At $x = 0$, the respective lengths of the Mn—O, Co—O, and Ni—O bonds are 0.1921, 0.1929, and 0.2045 nm, respectively. These are consistent with the atomic radii (0.053 nm for Mn^{4+}, 0.0545 nm for Co^{3+}, and 0.069 nm for Ni^{2+}). The small values of the Debye-Waller factor for Mn—O, Co—O, and Ni—O indicate the absence of Jahn-Teller active Ni^{3+} and Mn^{3+} ions in the pristine material. As the Li ions are deintercalated to the degree of charge state of $x = 1/3$ in $Li_{1-x}Ni_{1/3}Co_{1/3}Mn_{1/3}O_2$, the respective bond lengths of Mn—O and Co—O only slightly decrease from 0.1921 to 0.1914 nm and 0.1929 to 0.1914 nm, while the Ni—O bond length is drastically reduced from 0.2045 to 0.1931 nm. It indicates that Ni is the electroactive element. In addition, the Debye-Waller factor shows a maximum of 8.5×10^{-5} nm^2 for Ni—O ranging from $x = 0.25$ to 0.33. The change of Mn—O and Co—O is insignificant over the delithiated process. It suggests that Ni^{2+} ions are oxidized to Jahn-Teller active Ni^{3+} ions and the Mn and Co ions remain in the +4 and +3 states, respectively. This confirms the two-step redox reaction of Ni (i.e. Ni^{2+}/Ni^{3+} and

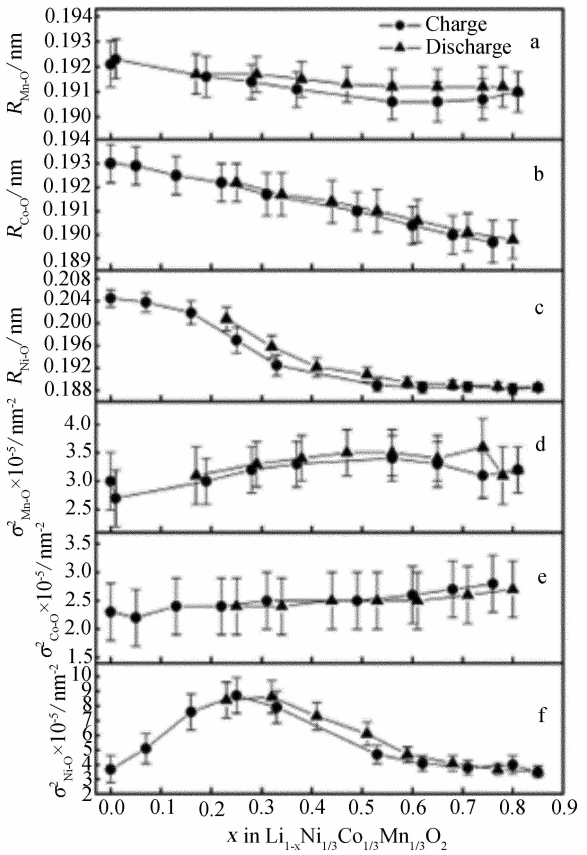

Fig. 9　The changes of structural parameters withdrawn from the first shell (Mn-O, Co-O, and Ni-O) of $Li_{1-x}Ni_{1/3}Co_{1/3}Mn_{1/3}O_2$ at various degree of charge states[12]

Ni^{3+}/Ni^{4+}) during cycling. Again Mn—O and Co—O show slight reductions in bond length from 1.914 to 0.1906 nm and from 0.1914 to 0.1901 nm, respectively; whereas, the Ni—O bond length varies from 0.1931 to 0.1891 nm, with x ranging from = 1/3 to 2/3. The significant changes of the Debye-Waller factor are observed for Ni—O as well, where the value decreases from 8.5×10^{-5} to 3.4×10^{-5} nm^2. This is in good agreement with the oxidation state of the Ni^{3+}/Ni^{4+} transition. A reverse trend is exhibited for the Debye-Waller factor of Ni—O, implying that the Jahn-Teller active Ni^{3+} concentration is highly related to the structural distortion of $Li_{1-x}Ni_{1/3}Co_{1/3}Mn_{1/3}O_2$.

3　Conclusion

The investigation of energy materials combined with an explanation of the electrochemical behavior and the developed XAS-based analysis provides a rich source of information for better understanding the fundamental processes involved. From the change of local

structures as well as the symmetry and valence states of the materials, the atomic-level environment of the materials can be depicted. The unique in situ analysis capability of XAS allows real-time understanding of the local electrochemistry taking place within the materials, which provides a fast and efficient probing tool. With knowledge combining electrochemistry and XAS, a better strategy may arise directed towards the improvement of electroactive materials, which may not be limited to energy applications.

Acknowledgement: The authors appreciate the long-term financial and technical supports from Science Council of Taiwan, Synchrotron Radiation Research Center of Taiwan and Taiwan University of Science and Technology.

参考文献(References):

[1] Hwang B J, Sarma L S, Chen J M, et al. Structural models and atomic distribution of bimetallic nanoparticles as investigated by X-ray Absorption Spectroscopy[J]. J Am Chem Soc, 2005, 127: 11140.

[2] Hwang B J, Kumar S M S, Chen C H, et al. Size and alloying extent dependent physiochemical properties of Pt-Ag/C nanoparticles synthesized by ethylene glycol method[J]. J Phys Chem C, 2008, 112: 2370.

[3] Hwang B J, Sarma L S, Wang G R, et al. Heat-induced alterations in surface population of metal sites in bimetallic nanoparticles[J]. Chem Eur J, 2007, 13: 6255.

[4] Lai F J, Sarma L S, Chou H L, et al. Architecture of bimetallic Pt_xCo_{1-x} electro-catalysts for oxygen reduction reaction as investigated by X-ray absorption spectroscopy [J]. J Phys Chem C, 2009, 113: 12674.

[5] Lai F L, Chou H L, Sarma L S, et al. Tunable physical properties of bimetallic Pt_xFe_{1-x} electro-catalysts as investigated by X-ray absorption spectroscopy and their catalytic activity toward oxygen reduction reaction[J]. Nanoscale, 2010, 2: 573.

[6] Lai F J, Su W N, Sarma L S, et al. Chemical dealloying mechanism of bimetallic Pt-Co nanoparticles and enhancement of catalytic reactivity toward to oxygen reduction reaction[J]. Chem Eur J, 2010, 16: 4602.

[7] Sarma L S, Chen C H, Yen S C, et al. Formation of Pt-Ru nanoparticles in ethylene glycol solution: an in situ X-ray absorption spectroscopy study [J]. Langmuir, 2009, 23: 5802.

[8] Hwang B J, Chen C H, Sarma L S, et al. Probing the formation mechanism and chemical states of carbon-supported Pt-Ru nanoparticles by in situ X-ray absorption spectroscopy[J]. J Phys Chem B, 2006, 110: 6475.

[9] Hwang B J, Sarma L S, Chen C H, et al. Controlled synthesis and characterization of Rucore-Ptshell bimetallic nanoparticles[J]. J Phys Chem C, 2008, 112: 19922.

[10] Hwang B J, Chen C H, Sarma L S, et al. Platinum-decorated ruthenium hexagonal nanostructures for the enhanced methanol electrooxidation [J]. Chem Cat Chem, 2009, 1: 1.

[11] Hwang B J, Sarma L S, Chen C H, et al. Depth-profile of alloying extent and composition in bimetallic nanoparticles investigated by in situ X-ray absorption spectroscopy[J]. Appl Phys Lett, 2007, 91: 023108.

[12] Tsai Y W, Hwang B J, Ceder G, et al. In situ X-ray absorption spectroscopic study on variation of electronic transitions and local structure of $LiNi_{1/3}Co_{1/3}Mn_{1/3}O_2$ cathode material during electrochemical cycling[J]. Chem Mater, 2005, 17: 3191.

以 X 光吸收光谱分析能源材料行为特性

郑铭尧[1], 潘俊仁[2], 郑如翔[2], 黄炳照[2,3*]

(1. 台湾科技大学工程技术研究所, 台湾 台北; 2. 台湾科技大学化学工程系, 台湾 台北;
3. 同步辐射研究中心, 台湾 新竹)

摘要: 本文介绍利用 X 光吸收光谱技术分析能源材料, 并以此分析技术, 了解材料中目标吸收元素之价数、d 轨域电子密度与局部环境变化, 深究能源材料之材料物化特性, 以藉此解释其电化学特性, 甚至做进一步之性能提升. 文中, 分别以燃料电池电极之电化学纳米触媒与锂电池电极材料为例, 说明 X 光吸收光谱技术之分析能力, 并与材料之电化学特性建立关联.

关键词: X 光吸收光谱; 纳米粒子; 双金属; 锂电池; 电极